NANO LETTERS

Letter

pubs.acs.org/NanoLett

Tin Anode for Sodium-Ion Batteries Using Natural Wood Fiber as a Mechanical Buffer and Electrolyte Reservoir

Hongli Zhu,[†,§] Zheng Jia,[‡,§] Yuchen Chen,[†] Nicholas Weadock,[†] Jiayu Wan,[†] Oeyvind Vaaland,[‡] Xiaogang Han,[†] Teng Li,*[,‡] and Liangbing Hu*[,†]

[†]Department of Materials Science and Engineering and [‡]Department of Mechanical Engineering, University of Maryland, College Park, Maryland 20742, United States

Supporting Information

ABSTRACT: Sodium (Na)-ion batteries offer an attractive option for low cost grid scale storage due to the abundance of Na. Tin (Sn) is touted as a high capacity anode for Na-ion batteries with a high theoretical capacity of 847 mAh/g, but it has several limitations such as large volume expansion with cycling, slow kinetics, and unstable solid electrolyte interphase (SEI) formation. In this article, we demonstrate that an anode consisting of a Sn thin film deposited on a hierarchical wood fiber substrate simultaneously addresses all the challenges associated with Sn anodes. The soft nature of wood fibers effectively releases the mechanical stresses associated with the sodiation process, and the mesoporous structure functions as an electrolyte reservoir that allows for ion transport through the outer and inner surface of the fiber. These properties are confirmed experimentally and computationally. A stable cycling performance of 400 cycles with an initial capacity of 339 mAh/g is demonstrated; a significant improvement over other reported Sn nanostructures. The soft and mesoporous wood fiber substrate can be utilized as a new platform for low cost Na-ion batteries.

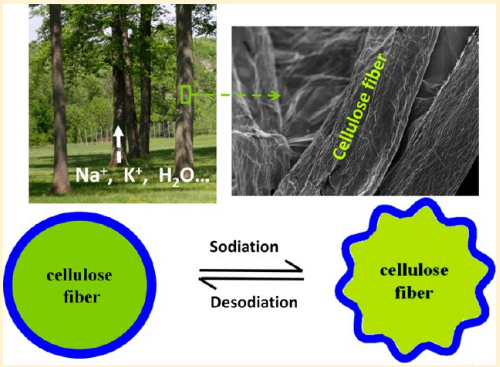

KEYWORDS: *Na-ion battery anode, Sn nanostructures, wood fibers, mechanical buffer, ion diffusion*

Grid scale storage is a crucial component of an energy landscape that incorporates a wide variety of renewable energy sources. Li-ion batteries and other electrochemical storage methods are considered among the most promising technologies for energy storage due to their high energy density and cyclability.[1−3] Grid scale storage requires a low cost, safe, and environmentally benign battery system. Na is an earth abundant material and Na-ion batteries fulfill these requirements better than Li-ion batteries. Widespread implementation of Na-ion batteries is limited by several factors: (1) slow Na ion diffusion kinetics, (2) large volume changes and structural pulverization during charging/discharging, and (3) difficulty in maintaining a stable solid electrolyte interphase (SEI).[4] These challenges are related to the large size of the Na ion (372% larger in volume than Li ion for a coordination number of four; R_{Li} = 59 pm, R_{Na} = 99 pm),[5] which makes it impossible to simply adopt the recent knowledge and strategies developed for high-performance Li-ion batteries. Several cathode materials and electrolyte systems have been studied for Na-ion batteries, including bilayered $Na_2V_2O_5$, P2 $Na_{0.66}Fe_{0.5}Mn_{0.5}O_2$, and fluorinated ethylene carbonate (FEC) as an electrolyte additive.[6−14] Anode materials that have been investigated include metal oxides and alloys, hard carbon, and nanocomposites.[9,15,16] Sn is a promising anode material because it alloys with Na at a high specific capacity of 847 mAh/g when $Na_{15}Sn_4$ is formed. Studies of Sn film and nanostructured anodes were reported; the cycle life, however, is limited to 20 cycles due to pulverization.[17−19] The pulverization is primarily due to a 420% volume expansion associated with the formation of $Na_{15}Sn_4$.[20] Recently developed Sn nanoforests and SnO_2@graphene nanocomposites improve cycling performance but lack the processability and cycling performance required for low cost grid scale storage.[21,22]

Wood naturally absorbs ions and water as part of the metabolism process. Specifically, this function is performed by wood fibers, or tracheids. The wood fibers are intrinsically soft, porous, and form into a multichannel structure.[23] In this study, we develop a nature inspired low cost electrode consisting of an electrodeposited Sn film on conductive wood fiber. Conductivity is achieved by a solution-based coating of carbon nanotubes (CNT) on the fiber surface. We find that the wood fiber increases the cyclability of Sn for Na-ion batteries by alleviating: 1) the capacity loss due to electrode pulverization, and 2) the poor rate performance as a result of slow ion diffusion kinetics. The stress reduction mechanism predicted by modeling the sodiation stresses throughout the Sn film on wood fiber agrees well with the experimental results. Control experiments with atomic layer deposition (ALD) confirm the role of the wood fiber as a mechanical buffer and electrolyte reservoir for ion diffusion. The Sn anode described is ideal for

Received: March 17, 2013
Revised: May 16, 2013
Published: May 29, 2013

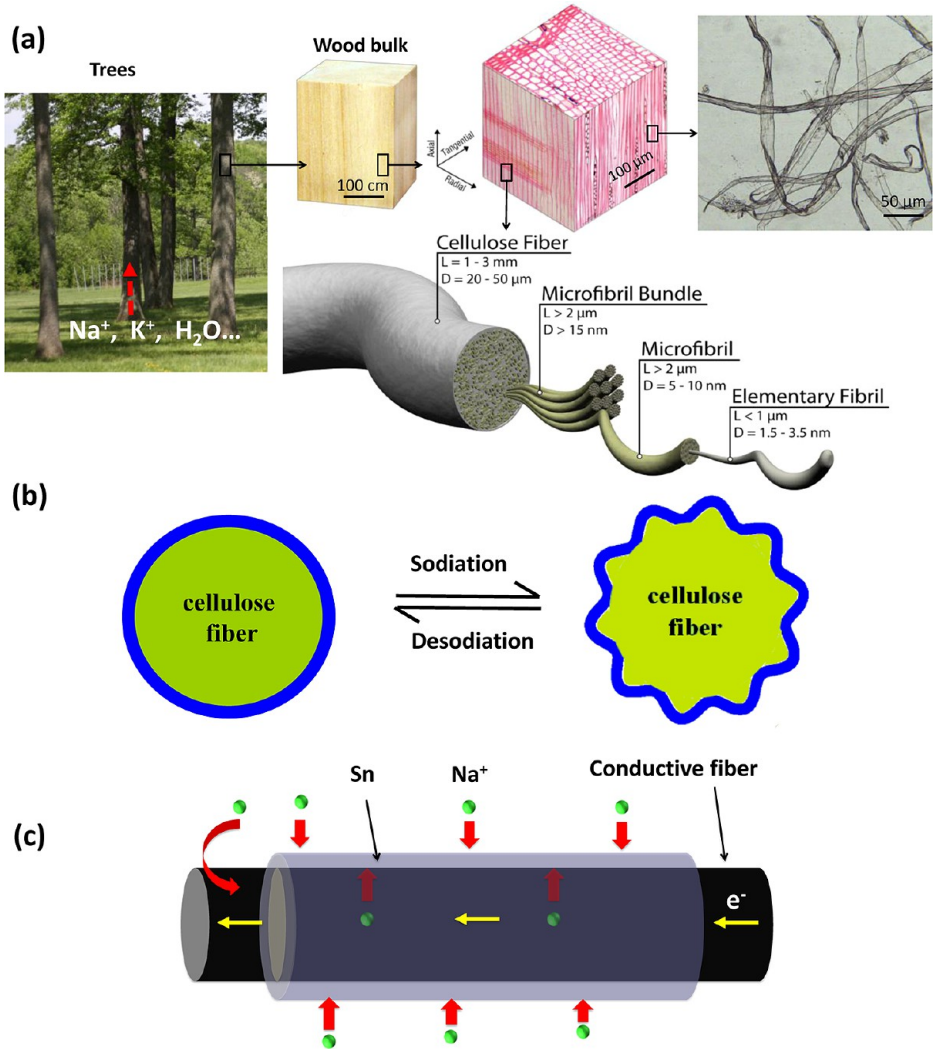

Figure 1. (a) Hierarchical structure of wood fiber. (b) Soft wood fiber substrates effectively release sodiation generated stresses by structural wrinkling. The thickness of Sn is 50 nm and the fiber diameter is ~25 μm. (c) Dual pathways for ion transport. The hierarchical and mesoporous structure of the fiber plays an important role as an electrolyte reservoir.

grid scale storage. The materials used are earth abundant and environmentally friendly, and electrodeposition and conductive fiber substrates are scalable for large throughput manufacturing.

Results and Discussion. The hierarchical structure of wood fibers, spanning the macroscale to the nanoscale, is illustrated in Figure 1a. Wood fibers are tracheids, hollow elongated cells that transport water and mineral salts. Pores in the fiber wall allow for intercellular fluid transportation.[23] One tracheid is comprised of thousands of microfibrils cellulose, creating a multichannel, mesoporous structure ideal for the absorption and transport of water and essential ions. Natural wood fibers with diameters on the order of 25 μm serve as the substrate for our Sn film. Compared to conventional rigid metallic substrates, the wood fiber is extremely soft. Initially, the fibers are coated with a thin layer (10 nm) of single-walled carbon nanotubes (SWCNTs) to provide electrical conductivity. Various other conductive materials, including graphene, metal nanowires, and conductive polymers could be deposited on wood fibers with similar solution-based processes.[24−26] Rich hydroxyl (−OH) groups on the cellulose surface provide strong hydrogen bonding between the fiber and conductive material. We predict that the soft substrate acts as a mechanical buffer during the sodiation/desodiation process. Figure 1b illustrates how the wood fibers release the stresses experienced by the Sn electrode. The substrate deforms together with the Sn film to release high stresses and prevent the delamination and pulverization characteristic of Sn anodes. Additionally, the wood fiber has a high capacity for electrolyte absorption. Liquid electrolytes penetrate the porous structure of the fiber, allowing for Na ion diffusion through the fiber cell walls in addition to diffusion at the Sn film surface, Figure 1c. This creates a dual ion transport path that effectively addresses the slow kinetics of Sn anodes for Na-ion batteries.

The effect of substrate stiffness on electrochemical performance is evaluated by comparing the cyclability of two Sn based electrodes, 50 nm Sn on wood fiber (Sn@WF) and 50 nm Sn on Cu. The areal mass of the Sn@WF is ~4 times greater than that on Cu due to the three-dimensional structure of the wood fiber substrate. Each electrode is tested in a half-cell configuration with a Na metal counter electrode and 1 M $NaPF_6$ in ethylene carbonate and diethyl carbonate (EC:DEC) electrolyte. Figure 2a plots the voltage profiles for the Sn@WF electrode at the first, second, 100th, and 400th cycle at a current density of 84 mA/g (C/10). Distinct plateaus at 0.18,

dx.doi.org/10.1021/nl400998t | Nano Lett. 2013, 13, 3093−3100

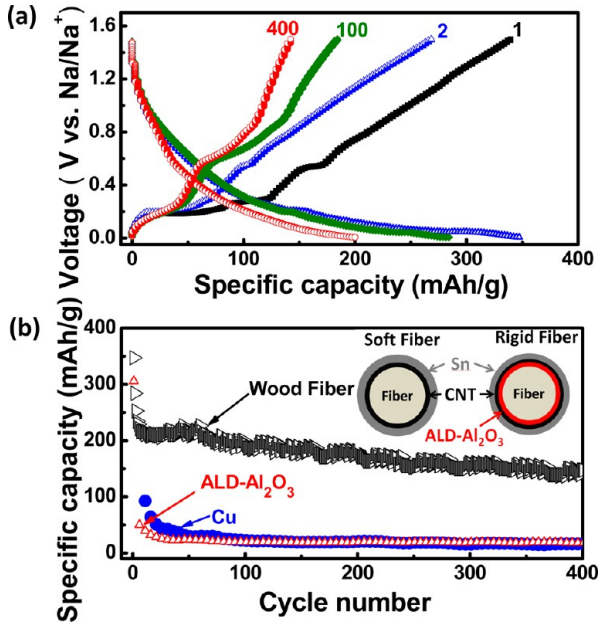

Figure 2. Electrochemical performance of the Sn anodes. (a) Galvanostatic charge/discharge voltage profiles of Sn@WF at the 1st, 2nd, 100th, and 400th cycle at a rate of C/10. (b) Cycling performance of Sn@WF, Al_2O_3 coated fiber, and Cu current collector at a rate of C/10. The inset illustrates the structure of the wood fiber and Al_2O_3 coated fiber.

0.27, 0.54, and 0.75 V versus Na/Na^+ are observed, corresponding to the formation of $Na_{15}Sn_4$, Na_9Sn_4, NaSn, and $NaSn_5$, respectively.[18] An initial discharge capacity of 339 mAh/g is achieved. After 400 cycles, the 0.18 and 0.54 V plateaus remain and the electrode maintains a capacity of 145 mAh/g. Note the first coulombic efficiency (CE) is still very low, 23%. We are continuing to improve CE by optimizing the electrolyte or modifying the Sn surface. The electrochemical performance of the Sn on Cu current collector is plotted in Figure S1 in the Supporting Information. Voltage plateaus at 0.18, 0.27, 0.54, and 0.75 V versus Na/Na^+ are initially observed with a capacity of 599 mAh/g. The capacity decreases to 97 mAh/g by the 10th cycle, and the voltage plateaus disappear after the 50th cycle. By the 100th cycle, the capacity decays to 22 mAh/g.

Figure 2b plots the specific capacity versus cycle number for Sn on three different substrates at a rate of C/10; natural wood fiber, Cu, and ALD Al_2O_3-coated wood fiber. The Sn@WF exhibits a lifetime of 400 cycles; among the longest cycling performance for Sn anodes in Na-ion batteries.[17,18] The capacity decayed during the cycling process, especially during the first few cycles. There are several potential explanations for this effect. Electrical contact between conductive fibers can be one possible reason. The initial volume changes associated with sodiation rearrange the fibers in such a way as to reduce the contact resistance at the intersection of two fibers. The decay rate reduces after the first a few cycles. Another possible mechanism for the faster initial decay is Sn locally cracking in some places along Sn@WF electrode; however cracking to the extent of complete pulverization is prevented by the fiber wrinkling. The third possible mechanism for the capacity decay includes loss of electrical contact between individual fibers and at the fiber−coin cell case interface. As a comparison, the usable lifetime of the other two substrates is only 10 cycles. Sn deposited on a rigid Cu substrate cracks and delaminates after the sodiation/desodiation process as a result of a large volume expansion.

We hypothesize that the dramatic increase in electrochemical performance is a result of the wood fiber acting as a mechanical buffer against sodiation induced stresses. It has been demonstrated that soft binders function as buffers to accommodate the mechanical stresses in batteries, effectively improving the device performance.[3,27] To prove this hypothesis, we intentionally introduce a stiff oxide layer between the wood fiber and SWCNT layer, maintaining all other parameters. As illustrated in Figure 2b, a 50 nm layer of Al_2O_3 is deposited via ALD to prevent any deformation of the fiber by the Sn film. The cycling performance of this control sample is similar to that of the Sn on Cu electrode. Stiffness measures the ability of a material to resist deformation under an external force; in this case the stresses associated with the sodiation of Sn. The circumferential stiffness of wood fibers ranges from 0.7−3.0 GPa, and the stiffness of Cu and Al_2O_3 is 102 and 375 GPa, respectively.[28,29] The low stiffness of the wood fiber releases the stresses induced during the charge/discharge cycling.

The morphology of the Sn@WF is characterized before and after galvanostatic cycling with a field emission scanning electronic microscope (FESEM). The cells were disassembled and washed in acetonitrile in the glovebox, then vacuumed dried and transferred into SEM for characterization. Figure 3a,c shows that the electrodeposited Sn initially forms a continuous nanoparticle film on the conductive wood fiber. The Sn nanoparticle thin film is in electrical contact with the SWCNTs that wrap the wood fibers. Typical sheet resistance of the conductive fiber current collector is ~30 Ohm/sq. After 400 cycles, the cell is disassembled at the fully sodiated stage, washed with acetonitrile, and examined in the FESEM. The formation of a wrinkled structure on all wood fibers is observed in Figure 3b,d. The wrinkling is associated with fiber deformation, resulting in the improved cycling performance. As shown in Figure 3d, no significant SEI layer is observed on the Sn@WF, a dramatic difference to the thick SEI observed on the Sn on Cu sample, Figure 3f. The lack of continuous SEI growth confirms the unique phenomenon of the mechanical stress release by wrinkling formation. The wrinkling deformation of the Sn film reduces rupturing of the SEI and exposure of the Sn to the electrolyte. The morphology of the Sn surface does not change after cycling, indicating the robustness of the structure on the wood fiber. The wrinkled structure aligns parallel to the long fiber direction. A similar wrinkling effect has been observed in Si anodes on a PDMS (polydimethylsiloxane) soft substrate for Li-ion batteries as a mean to effectively release stresses during cycling.[30−32] The morphology of the Sn on Cu current collector before and after cycling is presented in Figure 3e,f. The Sn particles expand and agglomerate upon cycling, resulting in pulverization and delamination of the film. The Sn volume expansion ruptures the SEI layer, and continuous exposure of the Sn electrode to the electrolyte results in further electrolyte decomposition and an increase in SEI layer thickness, a critical mechanism for capacity decay.[33]

Continuum chemomechanical modeling is performed with ABAQUS to investigate the morphology evolution of the Sn@WF during galvanostatic charging and discharging at the C/10 rate (see Supporting Information for details). The modeling results clearly confirm our hypothesis that the wood fibers act as a mechanical buffer (Figure 4, Figure S2 in Supporting

dx.doi.org/10.1021/nl400998t | Nano Lett. 2013, 13, 3093−3100

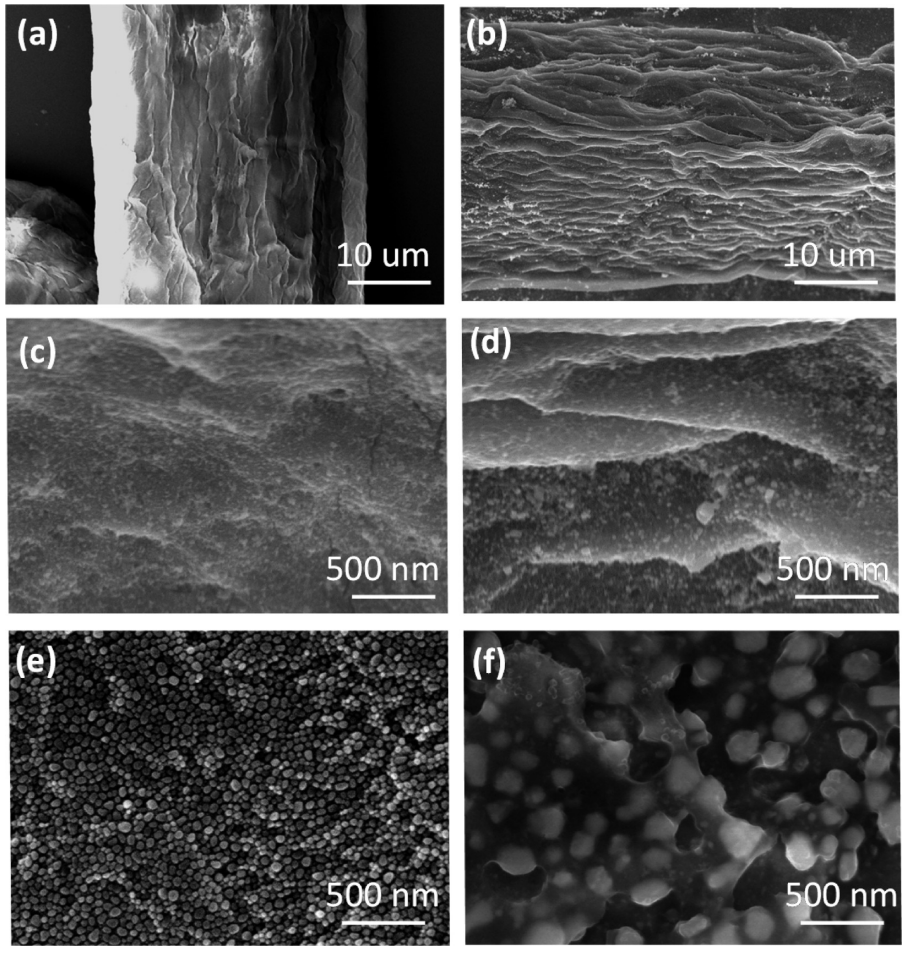

Figure 3. Sn@WF (a,c) before and (b,d) after 400 cycles at a rate of C/10. Sn on Cu current collector (e) before and (f) after 400 cycles. SEI formation and Sn volume expansion are clearly observed.

Information). As the system is charged, Na ions insert into the Sn and induce compressive stresses in the film. The compressive stress increases with the degree of sodiation. Given the large aspect ratio of the Sn film (50 nm over 10s of μm in circumferential length on wood fiber) and large Sn/wood fiber stiffness ratio, the initially smooth morphology of the thin Sn film becomes unstable and wrinkles when the compressive film stress is sufficiently high.

We define a normalized sodiation state (NSS) with NSS = 0 being the pristine unsodiated state and NSS = 1 the maximum sodiated state observed in the experiment. Simulations indicate that the Sn@WF begins to wrinkle at NSS = 0.4, and wrinkling increases with further sodiation. At the fully sodiated state, the wrinkle morphology is characterized by a wavelength of ~450 nm and an amplitude of ~70 nm (Supporting Information Figure S2), in good agreement with the experimentally observed wrinkled surface features in Figure 3b. The morphology at both the fully sodiated and fully desodiated states for the first cycle was examined. Two cells, one charged to 0.005 V versus Na/Na^+ and one charged to 0.005 V versus Na/Na^+ and then discharged to 1.5 V versus Na/Na^+, were disassembled in a glovebox for examination at the fully sodiated and desodiated state, respectively. The SEM images provided in Supporting Information Figure S5 clearly show that the sodiation-induced wrinkles are partially released after full desodiation. The mechanical modeling assumes an ideal initial Sn@WF structure with a perfectly cylindrical wood fiber and a smooth, uniformly thick Sn film. Real WFs have rough surface irregularities; we therefore do not expect a full release of the wrinkles in the Sn film to achieve a smooth surface morphology. By contrast, for a Sn film deposited on a stiff substrate (e.g., Al_2O_3 or Cu), film deformation is constrained to be rather uniform as any wrinkling deformation in the film would require distortion of the stiff substrate. As a result, Sn films on Al_2O_3 or Cu remain smooth during the sodiation process, and no wrinkling occurs (Supporting Information Figure S2d–f and Figure S4). Wrinkling of the Sn@WF reduces sodiation-induced deformations, effectively mitigating the associated stresses. Sn films supported by a stiff substrate must accommodate sodiation induced deformation via lattice distortion, resulting in a high film stress. Figure 4a and Supporting Information Figure S3a plot the Sn film morphology on the wood fiber and the contour of hoop stress $\sigma_{\theta\theta}$ (normal stress in the circumferential direction) in the Sn film at the fully sodiated and half sodiated states, respectively. Figure 4b plots the hoop stress distribution through the fully sodiated Sn film thickness at three representative locations: the crest (A), midpoint (B), and trough (C) of the wrinkle. For comparison, the hoop stress distribution in a fully sodiated Sn film supported by a stiff substrate is plotted in Figure 4b (see Supporting Information Figure S4 for details). The majority of sodiation-induced hoop stresses in the wrinkled Sn on wood fiber are significantly less than those in the smooth Sn film on a

dx.doi.org/10.1021/nl400998t | *Nano Lett.* 2013, 13, 3093–3100

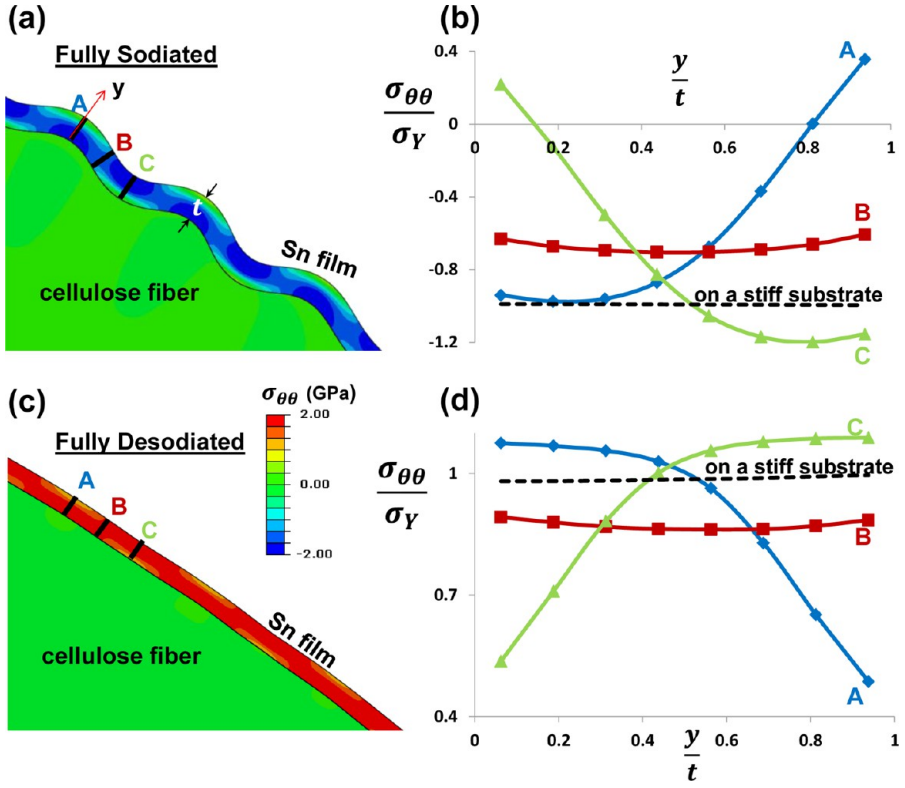

Figure 4. Chemomechanical modeling of the hoop stresses in Sn@WF at the fully sodiated (a) and desodiated (c) states. Color contours denote the hoop stress ($\sigma_{\theta\theta}$) level. The associated distributions of hoop stress normalized by yield stress versus location along film thickness are presented in (b) and (d). The hoop stress distributions for the Sn on a stiff substrate (Al_2O_3 or Cu) are denoted by the dashed line for comparison. The stress level comparison reveals that the wrinkling of Sn@WF effectively releases the sodiation/desodiation induced mechanical stresses.

stiff substrate. The maximum hoop stress at location B is 1.7 times less than in the stiff substrate-supported Sn film.

Modeling results further reveal that wrinkling of the Sn film on a soft cellulose fiber during sodiation half-cycle not only mitigates the sodiation-induced compressive stress but also plays a crucial role in reducing the tensile stress level in the Sn film during the desodiation half-cycle. It is this tensile stress that is the key driving force for Sn anode fracture during cycling. During discharging, Na ions are removed from the Sn@WF, smoothing out the wrinkling deformation. The Sn film recovers the rather smooth initial morphology after complete desodiation (Supporting Information Figure S2c and Figure 4c). Desodiation causes contraction of the Sn film; contraction that is constrained by the substrate. As a result, tensile hoop stresses accumulate in the Sn film during discharging. A high hoop stress could initiate and drive crack propagation through the Sn film, leading to the mechanical failure of the anode and capacity loss. In discharging the wrinkled Sn film from the fully sodiated state, smoothing of the wrinkled morphology partially accommodates the film contraction. Consequently, the resulting tensile stress after discharging is reduced. Stiff substrates (Al_2O_3 or Cu) also constrain the discharging-induced contraction in the Sn film. As shown in Figure 4c,d, the majority of tensile stresses of the Sn film supported by the wood fiber at full desodiation are effectively reduced. In comparison, high tensile stresses are apparent throughout the Sn film supported by a stiff substrate. In some locations on the Sn film supported by the wood fiber (e.g., near the interface at A or near surface at C), the tensile stress is moderately higher than for the stiff substrate-supported Sn film. The stresses are localized to an area half the thickness of the entire Sn film; the stresses in the other half of the film, however, are much less. This behavior is crucial to prevent crack propagation through the film. Cracks initiating from regions of high tensile stresses will not propagate through the entire Sn film due to an insufficient driving force in the low stress region. The overall structural integrity of the Sn film is preserved, ideal for high cycle performance. By contrast, the high tensile stresses in the Sn film supported by a stiff substrate are uniform through the entire film. Once cracks initiate, they will propagate through the film, pulverizing the Sn anode and reducing the active capacity and cycle performance.

The above chemomechanical modeling results reveal the following mechanistic understanding: a Sn@WF anode effectively releases the sodiation/desodiation-induced stresses via a wrinkling deformation. In particular, the reduced tensile stress during discharging prevents pulverization of the Sn anode, resulting in the significantly enhanced cycling performance evident in Figure 2b. Chemomechanical simulations with four different initial Sn film thicknesses, t_{Sn} = 50, 100, 150, and 200 nm are compared to investigate the effect of Sn mass loading on electrochemical performance. The evolution of the morphology and stress during a full sodiation/desodiation cycle of each of the four films are presented in the Supporting Information Figures S6 and S7. The maximum film thickness for theoretical modeling of Sn on the soft fiber is 200 nm. The stress mitigation effect of the soft wood fiber decreases as the thickness of the Sn film increases, largely due to the decreased wrinkle formation in the Sn film. These results suggest that a high mass loading may result in mechanical degradation and thus reduced electrochemical cycling performance of the Sn anode.

dx.doi.org/10.1021/nl400998t | *Nano Lett.* 2013, 13, 3093−3100

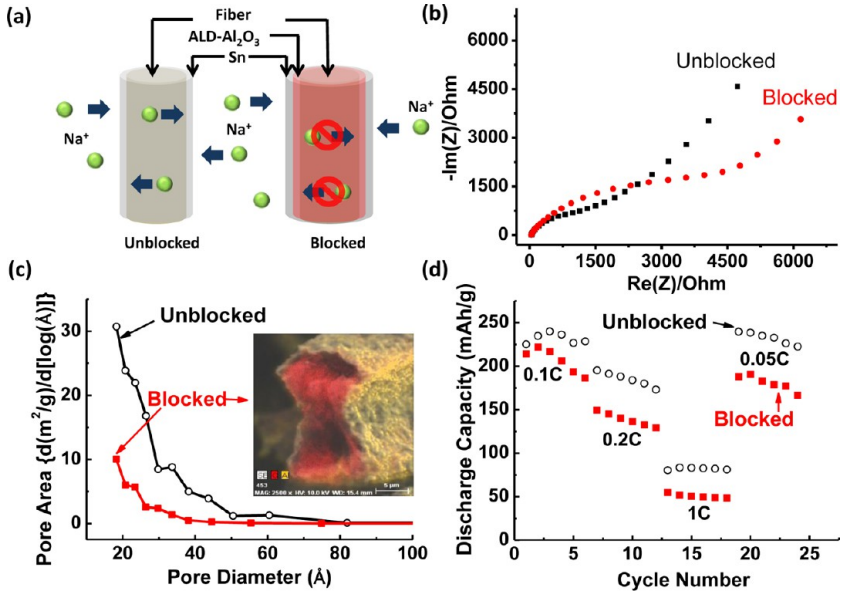

Figure 5. (a) Dual pathways for ion transport. Na ions transport along and diffuse through the mesoporous fiber structure. A conformal Al_2O_3 coating blocks the internal transport pathways. (b) EIS curves of samples with and without Al_2O_3 blocking. (c) BJH cumulative pore area $dA/d(\log D)$ vs pore diameter of the blocked and unblocked fiber samples. The inset SEM energy dispersive X-ray spectroscopy (SEM/EDX) element map confirms a conformal surface coating of 20 nm Al_2O_3 on the fiber. (d) Effect of mesoporosity of wood fibers on the rate performance of the Sn anode.

The performance of Na-ion batteries is also limited due to the slow transport kinetics associated with the large size of Na ions. Figure 5a illustrates how the internal porosity of the fiber doubles the number of Na ion transport paths to the Sn surface. The wood fiber functions as an electrolyte reservoir that provides the additional diffusion pathways. This property is confirmed with a control sample in which the fiber pores are blocked with a 20 nm ALD-Al_2O_3 coating, illustrated schematically in Figure 5a. The reason for reducing Al_2O_3 thickness to 20 nm is to minimize the effect of Al_2O_3 stiffness. Figure 5b plots the electrochemical impedance spectroscopy (EIS) curves of samples with and without the blocking layer, respectively. The internal resistance R_s of both samples is 46 ohms, which means the intrinsic resistance of the active material is not significantly affected by the Al_2O_3 coating. At medium frequencies, the diameter of the semicircle in the EIS curve corresponds to the charge transfer resistance at the electrode interface. The charge transfer resistance of the Al_2O_3 blocked sample is much larger than the bare sample, indicating that Na-ion transport is improved by dual pathway diffusion through Sn and mesoporous WF. The internal mesopore area of the fiber before and after Al_2O_3 coating is calculated from Brunauer–Emmet–Teller (BET) results in Figure 5c. The conformality of the ALD-Al_2O_3 coating is confirmed with energy dispersive X-ray spectroscopy (EDS) mapping. After the Al_2O_3 coating, the Barrett–Joyner–Halenda (BJH) adsorption cumulative pore area $dA/d(\log D)$ decreases dramatically from 30 to 10 $m^2/g{\cdot}Å$ at pore sizes ranging 20 to 80 Å. By reducing the fiber pore size, the Al_2O_3 coating reduces the electrolyte absorption capacity of the wood fibers and the fibers no longer function as an additional Na ion reservoir.

The electrochemical performance of the samples is characterized at different rates and the results are plotted in Figure 5d. The Al_2O_3 blocking layer reduces the performance of the Sn-fiber electrode. At higher rates of C/5 and 1 C, the capacity of electrodes without $A1_2O_3$ is nearly double that for the Al_2O_3 blocked electrodes. Note that a few precycles were carried out before the measurement for the comparison, which allow the electrolyte to have enough time to soak the electrodes. These results confirm that the wood fiber substrates effectively improve the rate performance of Na-ion batteries. The hierarchical wood fiber structure provides for high areal mass loading of the active material with just a thin Sn layer, decreasing the diffusion distance for Na ions.

Conclusions. The key metrics for Na-ion batteries are low cost and material abundance, as opposed to high-energy density for Li ion batteries. The target application for Na-ion batteries, therefore, is grid-scale energy storage. This removes some design constrains for materials and structures. The typical weight distribution ratio for electrode materials in batteries is as follows: active material to conductive additive to polymeric binder is 80:10:10, which provides for electrodes with high electronic conductivity, mechanical strength, and stability.[34] Large volume changes and stresses occur in high-capacity electrode materials; a higher weight percentage of binder is therefore preferred to improve the cycling performance. These inactive materials increase the total weight and cost of the battery and introduce inhomogeneous constituents to the electrode. We utilize electrochemical deposition to prepare a binder-free electrode consisting of a nanoparticle Sn thin film on a conductive wood fiber substrate/current collector. The active Sn maintains good electrical contact with the current collector, and the wood fibers provide a lightweight substrate with excellent mechanical properties, large surface area, and a porous structure that provides effective ion and electron transport.

A mechanical wrinkling effect releases mechanical stresses associated with the large volume change. Both experimental results and chemomechanical modeling prove that the extremely soft wood fiber effectively releases the mechanical stress generated during the sodiation/desodiation process. The mechanical properties of wood fibers result in unprecedented

dx.doi.org/10.1021/nl400998t | *Nano Lett.* 2013, 13, 3093–3100

cycling performance of Sn anodes for Na-ion batteries. The porosity of the wood fibers acts as an electrolyte reservoir, providing additional Na ion pathways to the Sn anode and improving the kinetics of Na ion transport. Blocking these pores greatly reduces electrochemical performance of these anodes. The abundance and large scale roll-to-roll processability of wood fibers make them an excellent candidate for energy storage applications where low costs are desired.

Experimental Section. *Conductive Cellulose Paper Fabrication.* Native wood fibers produced from southern yellow pine are dispersed in distilled water and stirred with an IKA RW20 digital mixer. A uniform fiber suspension is obtained and vacuum filtered through Buchner funnels with fritted discs. A wet sheet is formed and dried in an oven at 100 °C. The whole process is water based and additive free. P3 SWCNTs are purchased from Carbon Solutions (California). A sample of 1 mg/mL of SWCNT ink is prepared by adding 10 mg of SWCNTs to 10 mL of DI water with 1% SDBS, (4-dodecylbenzenesulfonic acid) bath sonicating 5 min, probe sonicating 3 min, and purifying with a centrifuge. The fiber sheet is immersed in the CNT ink for 2−3 min and dried in an oven at 100 °C. This procedure is repeated three times to achieve a sheet resistance of 30 ohms/square. Finally, the conductive fiber is washed with DI water to remove any residual surfactants.

Sn Electrodeposition. A conductive wood fiber working electrode is immersed in an electrolyte containing 0.012 g/mL of $SnSO_4$ (>95%, Sigma-Aldrich Inc.) and 0.4 g/mL of methanesulfonic acid (>99.5%, Sigma-Aldrich Inc.). Platinum metal serves as the counter electrode. A constant current of 0.5 mA is applied across the electrodes with an electrochemical potentiostat (VMP3, Biologic Inc.) for 15 min. A microbalance accurate to 0.01 mg (Citizen Scale Inc.) is used to determine the mass of the Sn.

Battery Assembly and Electrochemical Measurements. Half-cells composed of a Sn working electrode and solid Na metal (99%, Sigma-Alrich Inc.) counter electrode are assembled into coin cells for electrochemical characterization. The electrolyte is a solution of 1 M $NaPF_6$ (98%, Sigma-Aldrich) in ethylene carbonate and diethyl carbonate (EC/DEC 1:1 by volume). Separators and CR2032 coin cell cases were purchased from MTI, Inc. The electrochemical performance is tested with a Biologic VMP3 electrochemical potentiostat.

Atomic Layer Deposition. ALD coatings are performed in a commercial BENEQ TFS 500 reactor at 160 °C with trimethyl aluminum [TMA, $Al(CH_3)_3$] and DI water precursors. TMA and DI water are pulsed for 2 s each to improve the conformality of Al_2O_3 within the fiber mesopores. The 50 nm coating used as a mechanical buffer is deposited over a period of 500 cycles, and the 20 nm coating used in the ion diffusion study is deposited over 200 cycles, measured with a SOPRA GES5 spectroscopic ellipsometer.

Material Characterization. The surface morphology of the samples is observed in a field emission scanning electron microscope (SU-70, Hitachi Inc.) equipped with an energy dispersive X-ray spectrometer (EDS: Xflash6100, Bruker Inc.). The surface area and pore size of the samples are determined with a Micromeritics TriStar II 3020 Porosimeter Test Station. The range of measurable pore size is 17−1200 Å. The BET surface area (calculated from the linear part of the BET plot; P/P_0 = 0.06−0.20) and Barrett−Joyner−Halenda (BJH) adsorption average pore methods are used to evaluate the effect of the ALD Al_2O_3 coating. Chemomechanical modeling details are found in the Supporting Information.

■ ASSOCIATED CONTENT

Ⓢ Supporting Information

Additional information and figures. This material is available free of charge via the Internet at http://pubs.acs.org.

■ AUTHOR INFORMATION

Corresponding Author

*E-mail: (L.H.) binghu@umd.edu; (T.L.) LiT@umd.edu.

Author Contributions

§H.Z. and Z.J. contributed equally.

Notes

The authors declare no competing financial interest.

■ ACKNOWLEDGMENTS

We acknowledge the support of the Maryland Nanocenter and its Fablab and its Nisplab. The Nisplab is supported in part by the NSF as a MRSEC shared experimental facility. Z. Jia and T. Li acknowledge support by NSF Grants CMMI #1069076 and #1129826. L. Hu acknowledge the startup support from University of Maryland, College Park. We acknowledge Professor Chunsheng Wang for the use of the glovebox. We acknowledge Yuanyuan Li and Seongwoo Lee for their help in preparing schematics.

■ REFERENCES

(1) Yang, Z. G.; Zhang, J. L.; Kintner-Meyer, M. C. W.; Lu, X. C.; Choi, D. W.; Lemmon, J. P.; Liu, J. *Chem. Rev.* **2011**, *111* (5), 3577−3613.

(2) Chan, C. K.; Peng, H. L.; Liu, G.; McIlwrath, K.; Zhang, X. F.; Huggins, R. A.; Cui, Y. *Nat. Nanotechnol.* **2008**, *3* (1), 31−35.

(3) Kovalenko, I.; Zdyrko, B.; Magasinski, A.; Hertzberg, B.; Milicev, Z.; Burtovyy, R.; Luzinov, I.; Yushin, G. *Science* **2011**, *333* (6052), 75−79.

(4) Ong, S. P.; Chevrier, V. L.; Hautier, G.; Jain, A.; Moore, C.; Kim, S.; Ma, X.; Ceder, G. *Energy Environ. Sci.* **2011**, *4* (9), 3680−3688.

(5) Dean, J. A. *Lange's Handbook of Chemistry*, 15th ed.; McGraw-Hill: New York, 1999.

(6) Ponrouch, A.; Marchante, E.; Courty, M.; Tarascon, J.-M.; Rosa Palacin, M. *Energy Environ. Sci.* **2012**, *5* (9), 8572−8583.

(7) Komaba, S.; Ishikawa, T.; Yabuuchi, N.; Murata, W.; Ito, A.; Ohsawa, Y. *ACS Appl. Mater. Interfaces* **2011**, *3* (11), 4165−4168.

(8) Abouimrane, A.; Weng, W.; Eltayeb, H.; Cui, Y. J.; Niklas, J.; Poluektov, O.; Amine, K. *Energy Environ. Sci.* **2012**, *5* (11), 9632−9638.

(9) Cao, Y.; Xiao, L.; Sushko, M. L.; Wang, W.; Schwenzer, B.; Xiao, J.; Nie, Z.; Saraf, L. V.; Yang, Z.; Liu, J. *Nano Lett.* **2012**, *12* (7), 3783−3787.

(10) Kim, S.-W.; Seo, D.-H.; Ma, X.; Ceder, G.; Kang, K. *Adv. Energy Mater.* **2012**, *2* (7), 710−721.

(11) Palomares, V.; Serras, P.; Villaluenga, I.; Hueso, K. B.; Carretero-Gonzalez, J.; Rojo, T. *Energy Environ. Sci.* **2012**, *5* (3), 5884−5901.

(12) Komaba, S.; Murata, W.; Ishikawa, T.; Yabuuchi, N.; Ozeki, T.; Nakayama, T.; Ogata, A.; Gotoh, K.; Fujiwara, K. *Adv. Funct. Mater.* **2011**, *21* (20), 3859−3867.

(13) Tepavcevic, S.; Xiong, H.; Stamenkovic, V. R.; Zuo, X.; Balasubramanian, M.; Prakapenka, V. B.; Johnson, C. S.; Rajh, T. *Acs Nano* **2012**, *6* (1), 530−538.

(14) Yabuuchi, N.; Kajiyama, M.; Iwatate, J.; Nishikawa, H.; Hitomi, S.; Okuyama, R.; Usui, R.; Yamada, Y.; Komaba, S. *Nat. Mater.* **2012**, *11* (6), 512−517.

(15) Zhao, L.; Zhao, J. M.; Hu, Y. S.; Li, H.; Zhou, Z. B.; Armand, M.; Chen, L. Q. *Adv. Energy Mater.* **2012**, *2* (8), 962−965.
(16) Park, Y.; Shin, D.-S.; Woo, S. H.; Choi, N. S.; Shin, K. H.; Oh, S. M.; Lee, K. T.; Hong, S. Y. *Adv. Mater.* **2012**, *24* (26), 3562−3567.
(17) Xu, Y.; Zhu, Y.; Liu, Y.; Wang, C. *Adv. Energy Mater.* **2012**, 128−133.
(18) Chevrier, V. L.; Ceder, G. *J. Electrochem. Soc.* **2011**, *158* (9), A1011−A1014.
(19) Xiao, L.; Cao, Y.; Xiao, J.; Wang, W.; Kovarik, L.; Nie, Z.; Liu, J. *Chem. Commun.* **2012**, *48* (27), 3321−3323.
(20) Wang, J. W.; Liu, X. H.; Mao, S. X.; Huang, J. Y. *Nano Lett.* **2012**, *12* (11), 5897−5902.
(21) Liu, Y.; Xu, Y.; Zhu, Y.; Culver, J. N.; Lundgren, C. A.; Xu, K.; Wang, C. *ACS Nano* **2013**, *7* (4), 3627−3634.
(22) Su, D.; Ahn, H.-J.; Wang, G. *Chem. Commun.* **2013**, *49* (30), 3131−3133.
(23) Hon, D. N.-S.; Shiraishi, N. *Wood and Cellulosic Chemistry*, 2nd ed.; CRC Press: Boca Raton, FL, 2000.
(24) Weng, Z.; Su, Y.; Wang, D.-W.; Li, F.; Du, J.; Cheng, H.-M. *Adv. Energy Mater.* **2011**, *1* (5), 917−922.
(25) Hu, L.; Choi, J. W.; Yang, Y.; Jeong, S.; La Mantia, F.; Cui, L.-F.; Cui, Y. *Proc. Natl. Acad. Sci. U.S.A.* **2009**, *106* (51), 21490−21494.
(26) Carlsson, D. O.; Nystrom, G.; Zhou, Q.; Berglund, L. A.; Nyholm, L.; Stromme, M. *J. Mater. Chem.* **2012**, *22* (36), 19014−19024.
(27) Komaba, S.; Matsuura, Y.; Ishikawa, T.; Yabuuchi, N.; Murata, W.; Kuze, S. *Electrochem. Commun.* **2012**, *21* (0), 65−68.
(28) Cichocki, F. R.; Thomason, J. L. *Compos. Sci. Technol.* **2002**, *62* (5), 669−678.
(29) Tomioka, Y.; Yuki, N. *J. Mater. Process. Technol.* **2004**, *146* (2), 145−282.
(30) Iwamura, S.; Nishihara, H.; Kyotani, T. *J. Power Sources* **2013**, *222*, 400−409.
(31) Bhandakkar, T. K.; Johnson, H. T. *J. Mech. Phys Solids* **2012**, *60* (6), 1103−1121.
(32) Yu, C. J.; Li, X.; Ma, T.; Rong, J. P.; Zhang, R. J.; Shaffer, J.; An, Y. H.; Liu, Q.; Wei, B. Q.; Jiang, H. Q. *Adv. Energy Mater.* **2012**, *2* (1), 68−73.
(33) Wu, H.; Chan, G.; Choi, J. W.; Ryu, I.; Yao, Y.; McDowell, M. T.; Lee, S. W.; Jackson, A.; Yang, Y.; Hu, L.; Cui, Y. *Nat Nano* **2012**, *7* (5), 310−315.
(34) Sun, Y.-K.; Myung, S.-T.; Park, B.-C.; Prakash, J.; Belharouak, I.; Amine, K. *Nat. Mater.* **2009**, *8* (4), 320−324.

Supporting Materials

Tin Anode for Sodium-Ion Batteries Using Natural Wood Fiber as a Mechanical Buffer and Electrolyte Reservoir

Hongli Zhu,[1 (a)] Zheng Jia,[2 (a)] Yuchen Chen,[1 (a)] Nicholas Weadock,[1] Jiayu Wan,[1] Oeyvind Vaaland,[2] Xiaogang Han,[1] Teng Li,[2*] Liangbing Hu[1*]

Electrochemical Performance of Sn film on Cu substrate

The capacity decayed dramatically for the Sn thin film on a stiff Cu substrate. The discharge capacity is 98 mAh/g at the 10th cycle. It has two obvious plateaus at 0.27 V and 0.54 V and two short plateaus at 0.18 V and 0.75 V at the initial cycles. At the 50th cycle, these plateaus are not obvious any more. The discharge specific capacity is only around 22 mAh/g at the 100th cycle.

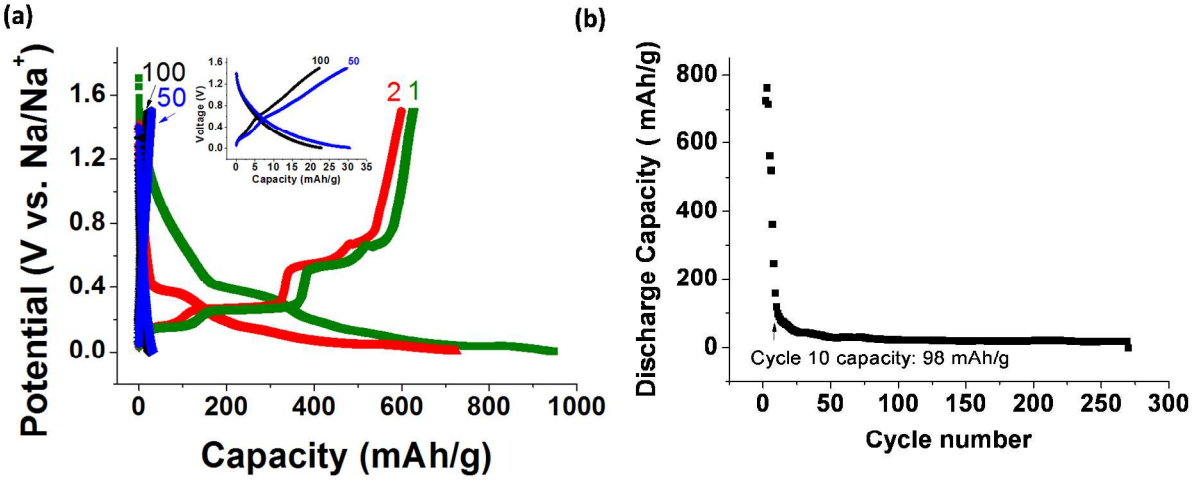

Fig. S1 Electrochemical performance of Sn thin film on hard Cu (a) Voltage profile of the 1st, 2nd , 50th and 100th cycle of Sn nanoparticle thin film on Cu foil at rate C/10 for Na-ion battery. Insert figure is the voltage profile of the 50th and 100th cycle. (b) Cycling performance of Sn thin film on hard Cu.

Methods for Simulation

To gain insights into the wrinkling phenomenon of Sn@WF observed during galvanostatic charge/discharge testing and its role on the better cycling performance of Sn@WF anode, we simulate the sodiation/desodiation (charging/discharging) process and the concurrent mechanical deformation through a fully coupled diffusion-displacement explicit analysis in commercial finite element code ABAQUS 6.10. The Sn film is initially pristine and subjected to a constant sodium flux I_0 at the surface under galvanostatic charging/discharging rate C/10. We employ a constant diffusivity $D = 10^{-14} cm^2/s$ to simulate the sodiation/desodiation process. During the course of charging/discharging, the sodiation state is characterized by how many Na ions are inserted into the tin anode. Here, we define a normalized sodiation state (NSS) as the current sodiation state divided by the maximum sodiation extent observed in the experiment and use it to characterize the charging/discharging state. According to the capacity measured from the experiment, NSS ramps from 0 up to 1 during charging half cycle and finally drops back down to 0 at the end of discharging half cycle. During cycling, Sn film undergoes plastic deformation to accommodate the large volumetric change (about 200%) induced by sodium insertion/extraction. An elastic-perfectly plastic constitutive law with Young's modulus of 40GPa and yielding stress σ_Y of 2GPa is assumed for sodiated Sn. Cellulose fiber is set to be a neo-Hookean material with Young's Modulus of 1.1GPa. Taking advantage of plane strain condition, only the circular cross section of the Sn@WF is simulated in order to reduce the computational cost. The diameter of cellulose fiber and initial thickness of pristine Sn film are $10\mu m$ and 50nm, respectively. The concurrent sodium diffusion and plasticity evolve the

wrinkling morphology of cellulose fiber supported Sn film and associated stress distribution.

Details of Simulation and Experimental Results

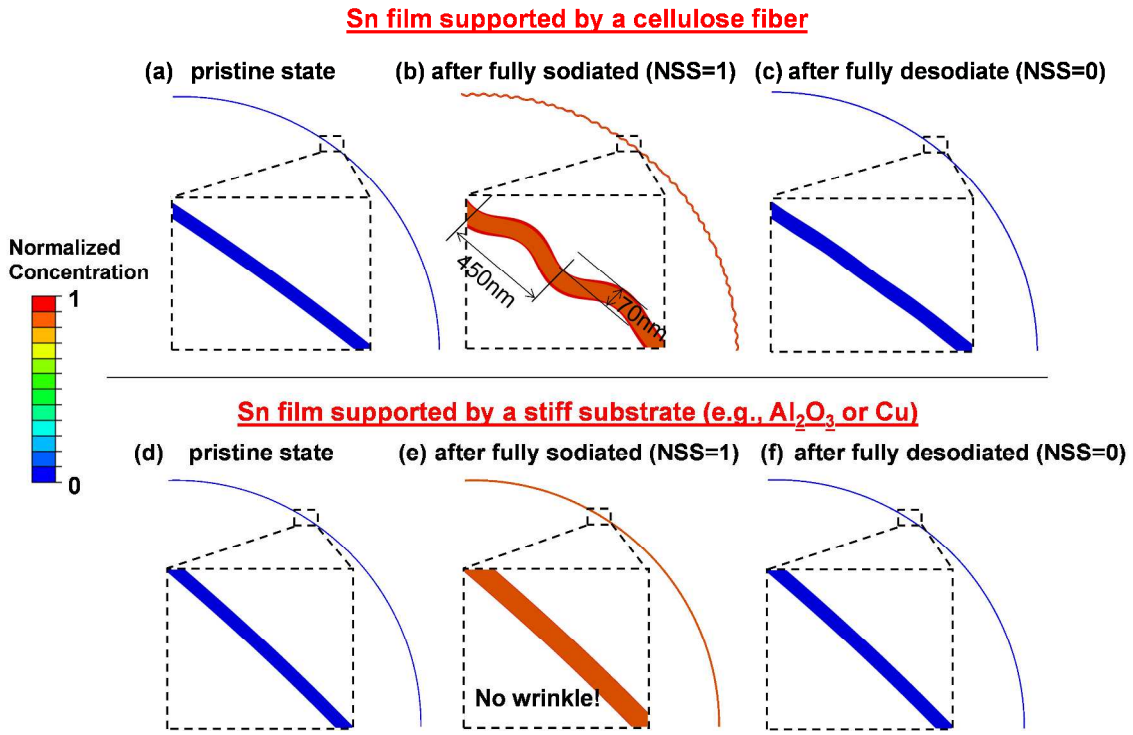

Fig. S2 Morphology evolution of Sn film on a cellulose fiber (a-c) versus that on a stiff substrate (e.g., Al_2O_3 or Cu) (d-f). For clarity, only part of the Sn film is shown here; the fiber and stiff substrate are not shown. (a-c) reveals that Sn@WF wrinkles during charging/discharging cycles. (a) pristine smooth Sn@WF. (b) after fully sodiated, cellulose fiber supported Sn film wrinkles. The wrinkle pattern is characterized by a wavelength of ~450nm and an amplitude of ~70nm. (c) after fully desodiated, wrinkling of the Sn film nearly disappears. (d-f) shows Sn film on a stiff substrate cannot wrinkle. (d) Pristine smooth Sn film on a stiff substrate. After fully sodiated (e)/desodiated (f), the Sn film remains the smooth morphology without wrinkling.

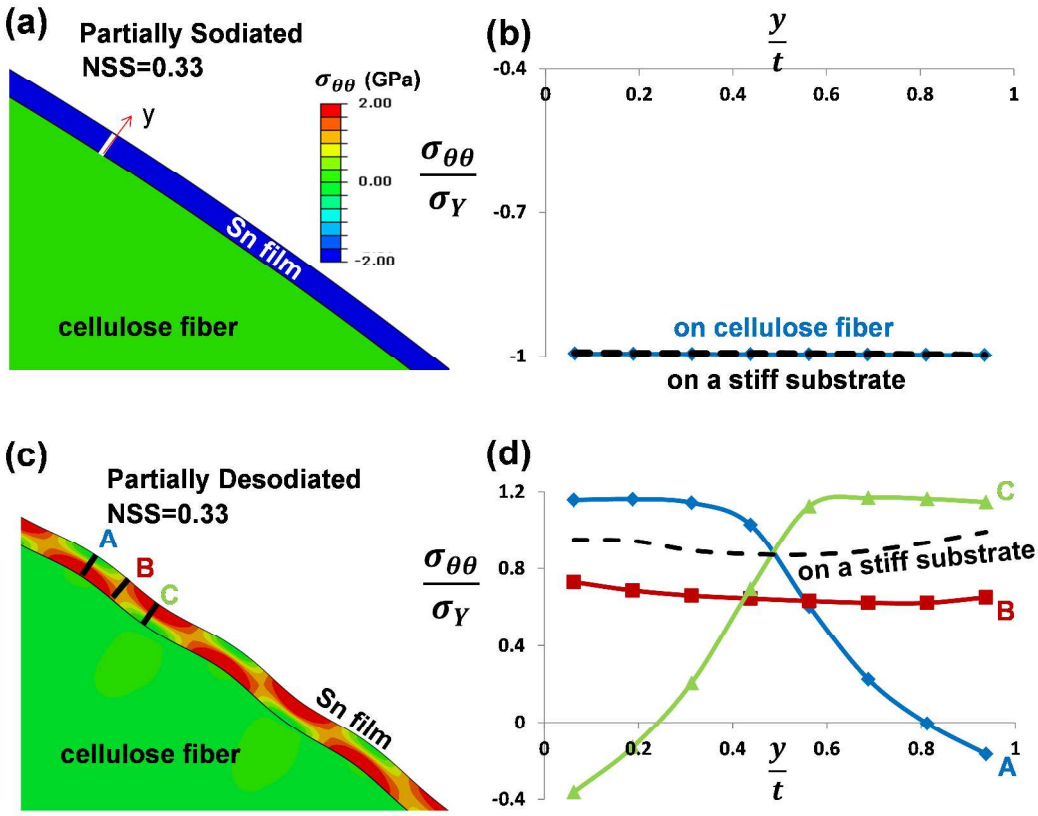

Fig. S3 (a) and (c) show morphology of a 50 nm Sn@WF at intermediate charging and discharging states ($NSS = 0.33$), respectively. Color contours denote the hoop stress ($\sigma_{\theta\theta}$) level. The associated distributions of hoop stress (normalized by yield stress) in the Sn film along thickness direction at three representative locations are plotted in (b) and (d), respectively. For comparison, dark dashed lines in (b) and (d) plot the hoop stress distribution in a Sn film supported by a stiff substrate.

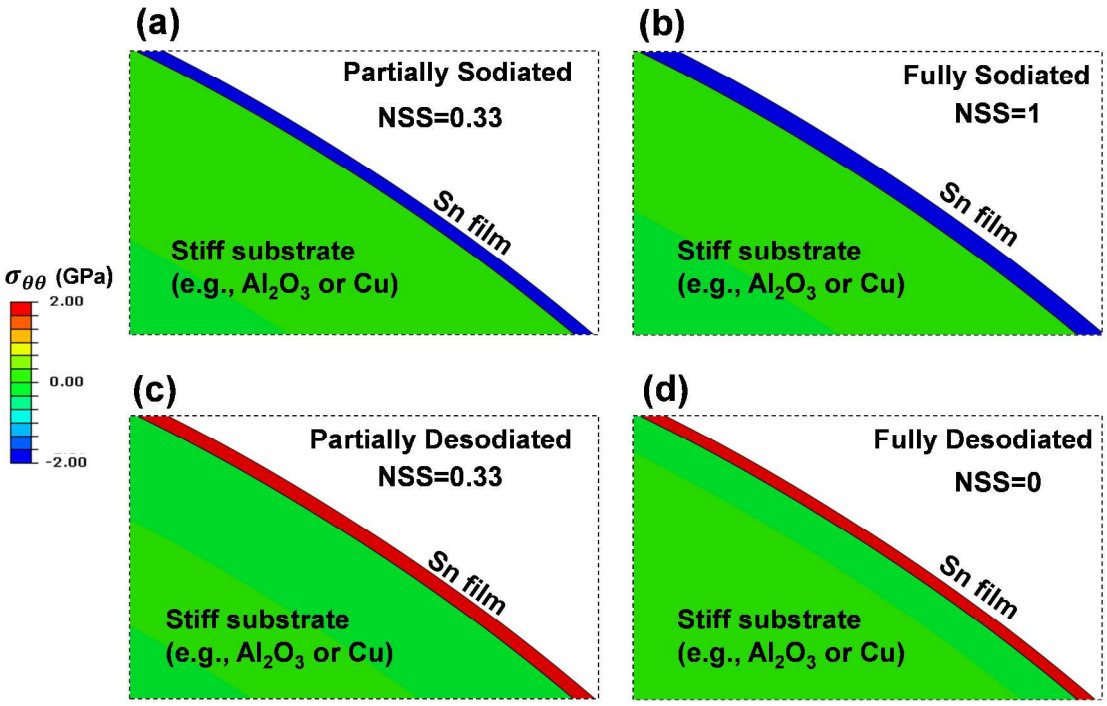

Fig. S4 Hoop stress distribution in stiff substrate supported Sn film during sodiation and desodiation. Hoop stresses in Sn film at (a) intermediate and (b) full sodiation stages are uniform and compressive (~-2GPa), but are tensile (~2GPa) at (c) intermediate and (d) full desodiation stages. Note the smooth morphology and high stress throughout the sodiation/desodiation cycle.

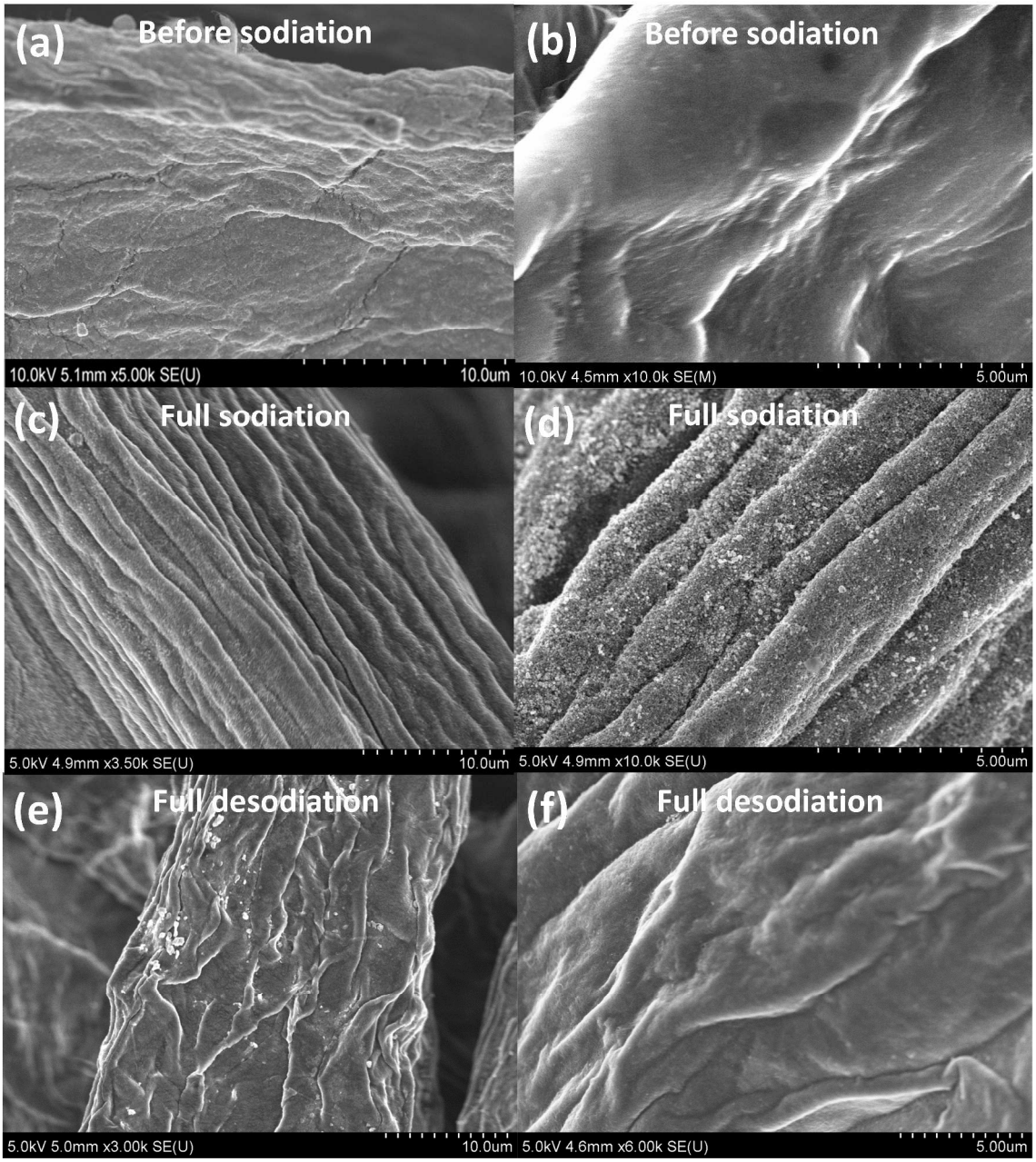

Figure S5: (a), (b) Experimental Scanning Electron Microscope (SEM) images of the morphology of the pristine electrode after electrochemical deposition; (c), (d) Experimental morphology of the fully sodiated electrode after the first half cycle; (e), (f) Morphology of the fully desodiated electrode at the end of the first cycle.

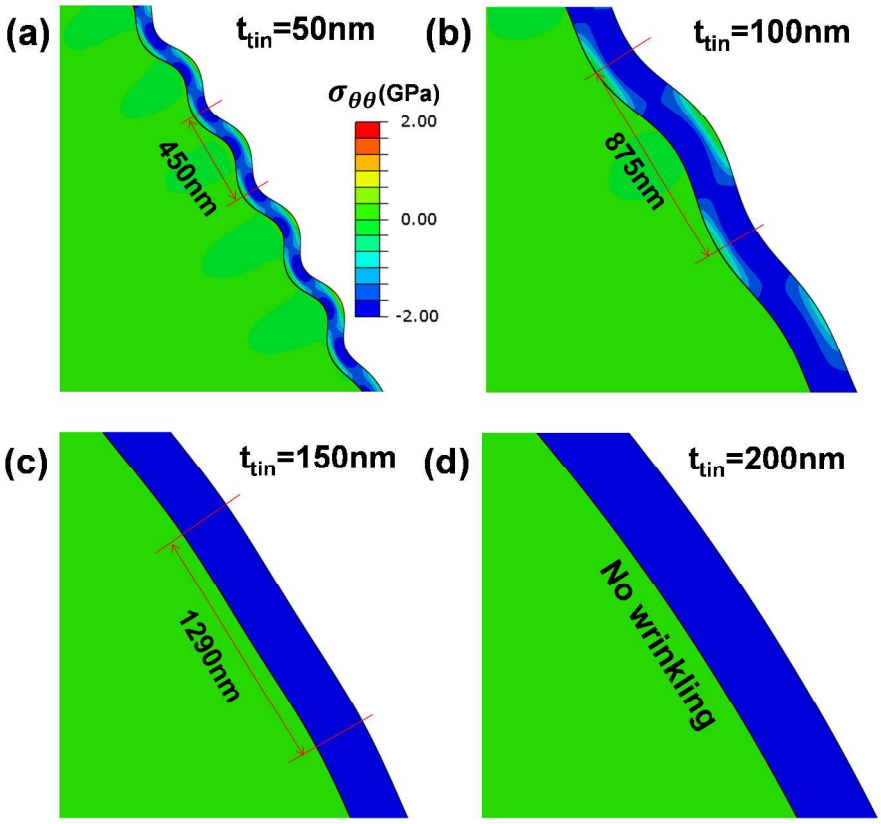

Figure S6. Morphology of cellulose fiber supported tin(Sn) films of various thicknesses (a) t_{tin} = 50nm, (b) 100nm, (c) 150nm, and (d) 200nm at the fully sodiated state. Color contours denote the hoop stress ($\sigma_{\theta\theta}$) level. As t_{tin} increases, the compression-induced wrinkling amplitude decreases and wrinkling wavelength increases. For a 200nm thick Sn film, no wrinkling occurs at full sodiation.

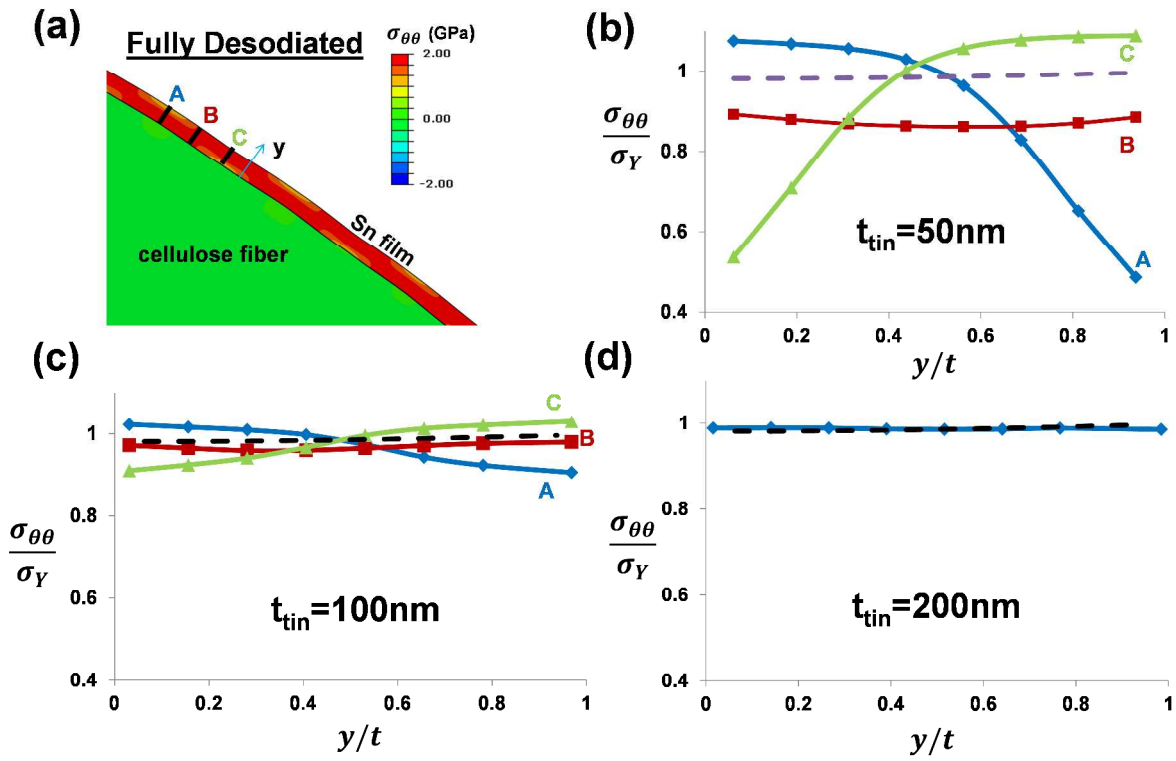

Figure S7. (a) Morphology of a cellulose fiber supported Sn film (50nm thick) at the fully desodiated state. Color contours denote the hoop stress ($\sigma_{\theta\theta}$) level. (b) Plots the associated distributions of hoop stress normalized by yield stress versus location along film thickness. Such distributions of hoop stress in a 100nm-thick and 200-nm thick Sn film are plotted in (c) and (d), respectively. As Sn film thickness increases, wrinkling formation during sodiation diminishes (as shown in Figure S5), which leads to less mitigation of desodiation-induced tensile stress. Without wrinkling (e.g., (d)), the tensile hoop stress is as high as that for an Sn film supported on a stiff substrate (denoted by the dashed line in each plot).